J Mater Sci (2013) 48:4143–4150
DOI 10.1007/s10853-013-7227-7

Synthesis and photocatalytic performance of the electrospun $Bi_2Fe_4O_9$ nanofibers

Shishun Qi · Ruzhong Zuo · Yu Wang · Helen Wong Lai-Wa Chan

Received: 16 December 2012 / Accepted: 6 February 2013 / Published online: 20 February 2013

Abstract $Bi_2Fe_4O_9$ nanofibers were successfully synthesized by an electrospinning method combined with a sol–gel process. The as-spun nanofibers were annealed at different temperatures ranging from 500 to 700 °C and a pure orthorhombic phase was obtained at 700 °C. The thermodecomposition behavior, structure, morphology, optical property, and the specific surface area of the nanofibers were characterized by thermogravimetry and differential scanning calorimetry, X-ray diffraction, field emission scanning electron microscopy, UV-vis diffuse reflectance spectroscopy and photoluminescene spectroscopy, and specific surface analyzer, respectively. The results indicated that the diameter and morphology of the fiber changed with different calcination temperatures. Moreover, the results of UV-vis diffuse reflectance spectroscopy revealed that the $Bi_2Fe_4O_9$ nanofiber could be a photocatalyst under a visible light irradiation and the bandgap value was determined to be 2.1 eV based on the Kubelka–Munk theory. The photocatalytic activity of the obtained nanofibers was evaluated by the degradation of methyl orange. A favorable degradation rate of 45 % was obtained for the sample annealed at 600 °C under the illumination of visible light for 3 h and an enhanced efficiency up to 70 % with recycling stability could be obtained with the aid of H_2O_2 for the pure-phase sample annealed at 700 °C. These results demonstrated that the electrospun $Bi_2Fe_4O_9$ nanofibers could be a promising visible light photocatalyst.

S. Qi · R. Zuo (✉)
Institute of Electro Ceramics & Devices, School of Materials Science and Engineering, Hefei University of Technology, Hefei 230009, People's Republic of China
e-mail: piezolab@hfut.edu.cn

Y. Wang · H. W. L.-W. Chan
Department of Applied Physics and Materials Research Center, The Hong Kong Polytechnic University, Hunghom Kowloon, Hong Kong, China

Introduction

Semiconductor photocatalysts have shown great potential in areas such as hydrogen production through photocatalytic water-splitting and photocatalytic remediation of harmful organics from water and air [1]. Of the semiconductor-based photocatalysts investigated, TiO_2 has received the most attention because of its good photocatalytic performance as well as its stability, nontoxicity, and availability [2]. However, TiO_2 could only respond to the ultraviolet (UV) light and its further applications in the visible light region are limited due to its relatively wide bandgap (3.2 eV) [3–5]. In order to make efficient use of the solar energy, various modifications such as doping with metal and non-metal elements have been applied to improve the photocatalytic activity of TiO_2 under visible light irradiation [6–8]. In recent years, more work is concentrated on the visible-light-driven photocatalysts, such as $CaBi_2O_4$, $BiFeO_3$, Bi_6WO_{12}, $SrTiO_3$–Fe_2O_3, etc., which have relatively small bandgap appropriate for the absorption of visible light [9–12]. $Bi_2Fe_4O_9$ has been an important material as gas sensors and catalysts for the ammonia oxidation to NO, showing great potential to replace the high-cost commercial catalysts (platinum, rhodium, and palladium alloys) in the industrial process of nitric acid manufacturing [13–16]. Recently, it has been reported that $Bi_2Fe_4O_9$ can be considered as a spin-frustrated multiferroic material and shows magnetodielectric effects close to room temperature [17–19]. For the photocatalytic applications, $Bi_2Fe_4O_9$ has been demonstrated to be a semiconductor with a bandgap around 2.1 eV and showed

oxidative decomposition ability over different kinds of organic contaminants under UV and visible light [20–24]. Furthermore, the morphology and crystal size of $Bi_2Fe_4O_9$ were reported to have a great influence on the photocatalytic oxidation behavior [20, 24]. Moreover, a recent study showed that the Al substitution in the $Bi_2Fe_4O_9$ could enhance the photocatalytic activity [25].

According to the literature survey, $Bi_2Fe_4O_9$ with a few kinds of morphologies have been synthesized through various processing methods, such as submicron cubes through molten salt technique [16], nanoparticles or microparticles through sol–gel method [22, 26, 27], and flowerlike microplates and nanosheets through hydrothermal method [20, 21, 28]. To the best of our knowledge, $Bi_2Fe_4O_9$ nanowires were only prepared through a multistep template-derived route and no further investigation of the relevant property [29]. There have been so far no other reports on the fabrication and photocatalytic property of this promising photocatalyst with one-dimensional structure.

Electrospinning has been demonstrated to be a simple, versatile method to synthesize continuous nanofibers of different compositions [30–35]. Mesoporous nanofiber membranes have already been prepared for water purification through this technique [36–39]. In the present work, the $Bi_2Fe_4O_9$ nanofibers synthesized through electrospinning were reported for the first time. The diameter and morphology of the fibers were found to have a strong dependence on the annealing temperature. The optical properties together with the photocatalytic activity of the electrospun $Bi_2Fe_4O_9$ nanofibers over the methyl orange (MO) were systematically studied. Favorable efficiency with good recycling stability was obtained for the synthesized pure-phase $Bi_2Fe_4O_9$ nanofiber. The results indicated that $Bi_2Fe_4O_9$ nanofibers prepared by electrospinning had efficient degradation capacity to MO under visible light irradiation.

Experimental procedure

$Bi_2Fe_4O_9$ nanofibers were prepared by electrospinning combined with a sol–gel method. First, a sol–gel solution, referred to as solution A, was prepared by dissolving 3.027 g of Bi $(NO_3)_3{\cdot}5H_2O$ and 4.848 g of Fe $(NO_3)_3{\cdot}9H_2O$ in 22 ml of 2-methoxyethanol (2-MOE, self-ionization constant $\sim 3 \times 10^{-6}$). The pH value of the solution was adjusted to be 4.0 by adding drops of ethanolamine. Then, 6 ml of glacial acetic acid was added to control the solution viscosity. The solution was stirred for 12 h at room temperature. Second, solution B was prepared by adding 1 g of polyvinyl pyrrolidone (PVP, $M_w = 1\ 300\ 000$) to 10 ml of dimethyl formamide (DMF)/ethanol (1:1) solvent mixture. The solution B was magnetically stirred for 1 h after the PVP was dissolved. Third, 5 ml of solution A was added to the solution B drop by drop under continuous stirring and the homogeneous $Bi_2Fe_4O_9$ precursor solution for electrospinning was obtained. All the raw materials were of analytic purity without further purification.

In a typical electrospinning process, the precursor solution was loaded into a plastic syringe and fed by a micro-infusion pump to the stainless steel needle. The electrospinning setup we used was a horizontal one with a rotating drum as a collector [40]. A high voltage of 16 kV was supplied by a direct-current power supply and the feeding rate was adjusted to be 0.4 ml/h. The distance was 14 cm from the needle to the collector which was wrapped by the alumina foil. After the electrospinning process, the fiber mats could be collected on the aluminum foil. The as-spun nanofibers were placed in a muffle furnace and calcined in air for 2 h at different temperatures ranging from 500 to 700 °C at a heating rate of 1 °C/min.

Thermogravimetry (TG) and differential scanning calorimetry (DSC) analysis of the as-spun $Bi_2Fe_4O_9$/PVP composite nanofibers was carried out to study the thermodecomposition behavior using a simultaneous thermal analyzer (STA409C, Netzsch, Germany). The phase structure of the sample was characterized by an X-ray diffractometer (XRD, D/Max-RB, Shimadzu, Japan) with Cu Kα line of 0.1541 nm. A field emission scanning electron microscope (FE-SEM, Sirion200, FEI, USA) was used to observe the morphologies of the nanofibers. Ultraviolet-visible (UV-vis) diffuse reflection spectrum was measured on a UV-vis spectrometer (TU-1950, Beijing Purkinje General Instrument Co., Ltd, Beijing, China) and the band gap of the $Bi_2Fe_4O_9$ fibers was calculated through the Kubelka–Munk method. The specific surface areas of the as-prepared samples were determined according to the Brunauer–Emmett–Teller (BET) method on nitrogen adsorption at 77 K using a TriStar II 3020M analyzer (Micromeritics Co., USA). The room temperature photoluminescence spectra were measured on a fluorescence spectrophotometer (F-4600, Hitachi, Japan).

The photocatalytic activity of $Bi_2Fe_4O_9$ nanofibers was evaluated by the degradation of MO under the irradiation of a 400 W metal-halide lamp ($\lambda > 380$ nm) at natural pH value. For the degradation of MO, the initial concentration of MO was 20 mg/L with a photocatalyst loading of 1 g/L. First, the solution was stirred in the dark for 30 min to obtain a good dispersion and reach adsorption–desorption equilibrium between the organic molecules and the catalyst surface. After every 1 h, a small quantity of the solution was taken, and the concentration of MO was determined by comparing the absorbance at 464 nm, which was measured by the UV-vis spectrophotometer. Each time before the measurement, the sample solution was centrifuged at 4000 rpm/min for 20 min to separate the catalyst from the

solution. For the determination of the cycling properties, the catalyst in the solution was precipitated, taken out, and dried. The obtained catalyst was used for the next photocatalytic reaction.

Results and discussion

The thermal analysis of the as-spun $Bi_2Fe_4O_9$/PVP composite fiber is shown in Fig. 1. Below 250 °C, there was a weight loss about 20 %, which was indicative of the volatilization of the adsorbed water and the residual solvent in the fiber. Then, a sharp weight loss of about 40 % could be observed in the TG curve between 250 and 300 °C, accompanied by two exothermal peaks at 259 and 285 °C, respectively. The strong exothermal peak at ~259 °C could be ascribed to the partial decomposition of PVP and the peak at ~285 °C was assigned to the decomposition of the nitrates. When the temperature was further increased from 300 to 400 °C, a weight loss of 20 % could be detected from the TG curve accompanied by a strong exothermal peak at 375 °C in the DSC curve. The strong exothermal peak in the DSC curve could be assigned to the total decomposition of the residual nitrates and organic matters in the fiber. Above 500 °C, no weight loss could be detected and a weak exothermal peak could be observed in the inset figure of Fig. 1, which could be ascribed to the crystallization behavior of the $Bi_2Fe_4O_9$.

The purity and crystallinity of the electrospun nanofibers after calcination were examined by X-ray diffraction (XRD). Fig. 2 shows the XRD patterns of the as-prepared $Bi_2Fe_4O_9$ nanofibers annealed at different temperatures. After annealing at 500 °C, the main phase of the sample was indexed to be $BiFeO_3$ (JCPDS 20-0169) with only traces of $Bi_2Fe_4O_9$ (JCPDS 25-0090). However, when the annealing temperature increased from 550 to 650 °C, the main phase was transformed to the orthorhombic-structured $Bi_2Fe_4O_9$, except for traces of $BiFeO_3$ which could be detected from the diffraction peak around 32°. Pure-phase $Bi_2Fe_4O_9$ was found to appear after annealing at 700 °C. After the refinement, the cell constants of $Bi_2Fe_4O_9$ annealed at 700 °C were calculated to be $a = 7.97$ Å, $b = 8.45$ Å, and $c = 6.01$ Å, which are in agreement with the standard data of $Bi_2Fe_4O_9$ (JCPDS 25-0090). It could also be noted from Fig. 2 that the crystallinity of the nanofibers was enhanced with the increment of the annealing temperature, because the diffraction peaks became strong and narrow. There are only traces of $BiFeO_3$ in the samples annealed at 600 and 650 °C, so the two samples were also used for comparison in the following investigation.

The typical SEM images of the electrospun $Bi_2Fe_4O_9$/PVP nanofibers before and after the heat-treatment are displayed in Fig. 3a–d. It can be observed from Fig. 3a that the obtained polymeric fibers exhibit smooth surfaces due to the amorphous nature of the PVP. The fiber diameter was uniform and the average value was about 320 nm determined by measuring tens of fibers. These fibers were ultra long and in a random orientation, which was caused by the instability of the spinning jet. As shown in many researches, the morphology of the nanofibers was strongly affected by the heat-treatment procedure. Different morphologies of the fibers were obtained by annealing at different temperatures of 600, 650, and 700 °C, which could be clearly seen from Fig. 3b–d. During sintering, the formation of orthorhombic phase $Bi_2Fe_4O_9$ fibers from the composite fibers should involve at least three processes: thermal-decomposition of the polymer (PVP), nucleation of $BiFeO_3$ and then the transformation to $Bi_2Fe_4O_9$, and directional mass transport of $Bi_2Fe_4O_9$ nanocrystals to form continuous nanofibers. Due to the removal of the

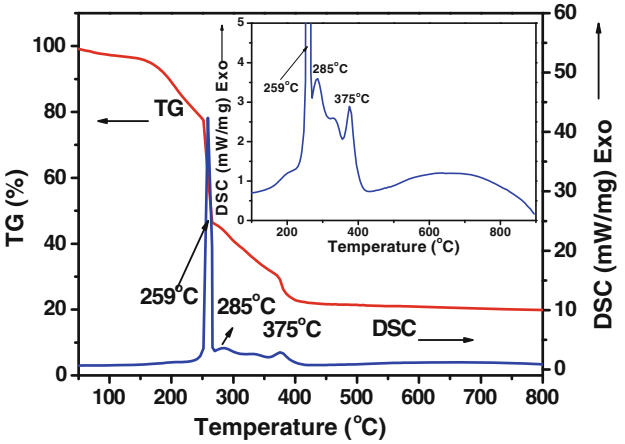

Fig. 1 DSC/TG curves of the as-spun PVP/$Bi_2Fe_4O_9$ composite nanofibers. The *inset* figure is a magnified DSC curve

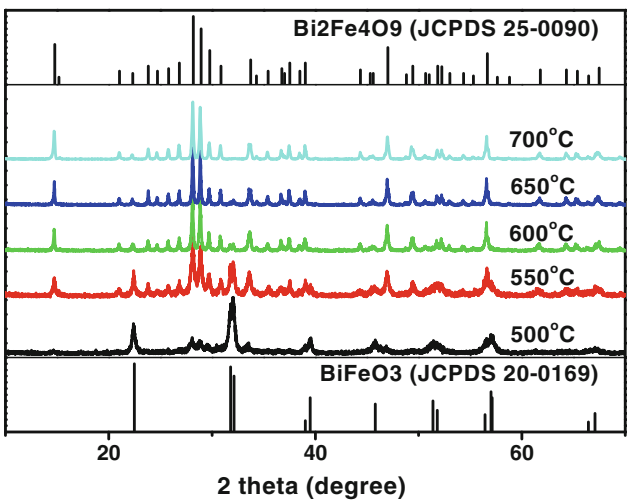

Fig. 2 XRD patterns of the $Bi_2Fe_4O_9$ nanofibers annealed at different temperatures as indicated

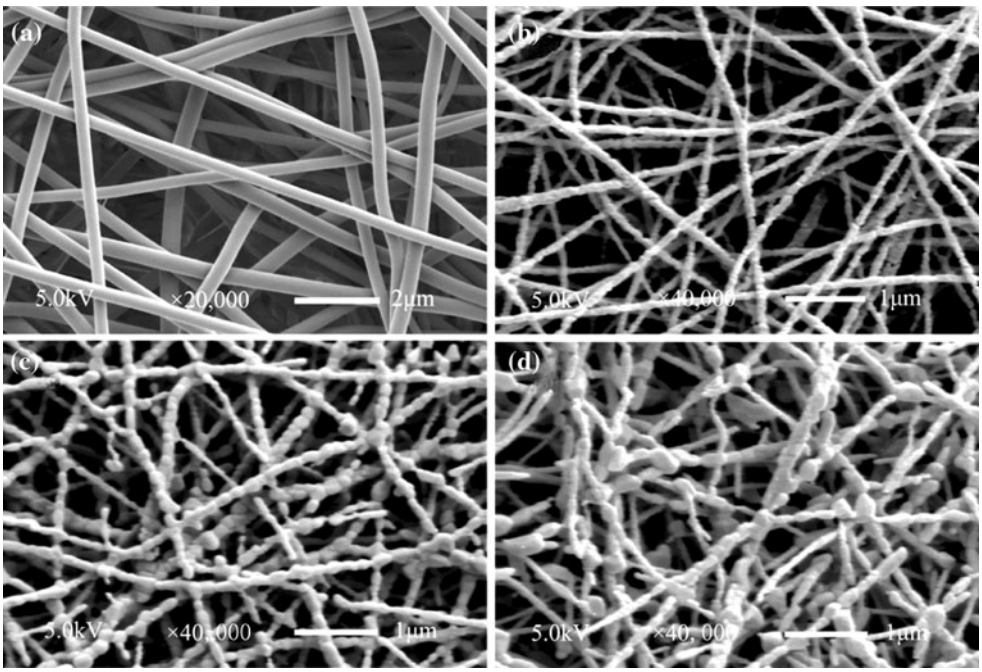

Fig. 3 SEM images of the $Bi_2Fe_4O_9$ nanofibers before and after the calcination **a** the as-spun nanofibers, **b** annealed at 600 °C, **c** annealed at 650 °C, and **d** annealed at 700 °C

polymer (PVP) and other organic components in the fiber, the fiber diameter was reduced to 150 nm and 180 nm after annealing at 600 and 650 °C, respectively. As shown in Fig. 3b, c, the fiber remained continuous after the crystallization of the $Bi_2Fe_4O_9$. However, the surface became rougher when the annealing temperature was increased from 600 to 650 °C, which could be mainly assigned to the transformation of the $BiFeO_3$ phase as detected in the XRD results and the crystallization behavior of the $Bi_2Fe_4O_9$. When annealing at 700 °C, the fibers became coarsened and the diameter was increased to 250 nm. In addition, some fibers were broken into shorter fibers and some particle-chain like structures appeared, which could be clearly observed from Fig. 3d. The increment of the fiber diameter and the coarseness of the surface could be mainly assigned to the crystallization behavior of the $Bi_2Fe_4O_9$ and the directional mass transport in the $Bi_2Fe_4O_9$ nanofibers. Along with the mass transport, the total transformation of the BiFeO3 phase might also contribute to the coarseness of the fiber surface. Besides, the fiber break at some points could be mainly assigned to the stress which was caused by the directional mass transport.

As for a photocatalyst, it is essential to investigate the optical absorption for the study of the relevant photocatalytic performance. Figure 4a exhibits the optical absorption spectra of the as-prepared $Bi_2Fe_4O_9$ nanofibers annealed at different temperatures. The three curves of the absorption spectra show a similar shape, in which two absorption edges could be detected. The first absorption edge was above 600 nm and the other was above 800 nm. These two values were consistent with those reported previously [21, 24]. The former could be ascribed to n–p or p–p electronic transitions, while the latter probably resulted from the d–d electronic transitions of Fe. At the same time, the first absorption edges above 600 nm indicated that the three samples could respond to the light from UV light region to visible light region. The nanofibers annealed at 700 °C showed higher absorption intensity in the wavelength range smaller than 500 nm. The higher absorption intensity could be assigned to the better crystallization of the nanofibers annealed at 700 °C, which was consistent with the XRD results. As known, optical absorption properties of a photocatalyst are closely related to its optical energy gap. For determining the bandgap value of the obtained $Bi_2Fe_4O_9$ nanofibers, the square root of the Kubelka–Munk (K–M) functions $(F(R)*h\nu)^{1/2}$ was plotted against the photo energy ($h\nu$), as shown in Fig. 4b [7, 11, 41, 42]. When the tangent lines were extrapolated to $(F(R)*h\nu)^{1/2}= 0$, the bandgap value could be obtained. It can be seen that $Bi_2Fe_4O_9$ nanofibers annealed at different temperatures exhibited a similar bandgap value around 2.1 eV. Such a bandgap value is much smaller than that of the popular photocatalyst TiO_2 (3.2 eV), indicating a possibility of utilizing more visible light for photocatalysis.

The photocatalytic activity of $Bi_2Fe_4O_9$ nanofibers was evaluated by the degradation of a typical organic contaminant MO under the visible light irradiation. Figure 5 displays the photo-degradation efficiencies of MO as a function

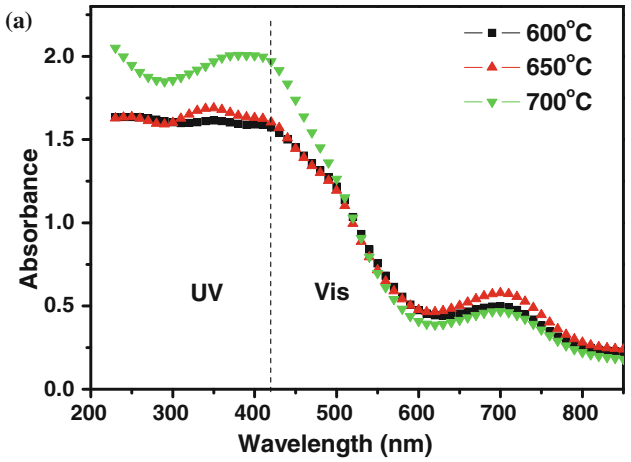

Fig. 4 **a** UV-vis optical absorption spectra of the $Bi_2Fe_4O_9$ nanofibers annealed at different temperatures, and **b** Plots of $(F(R)h\nu)^{1/2}$ versus the energy of absorbed light ($h\nu$)

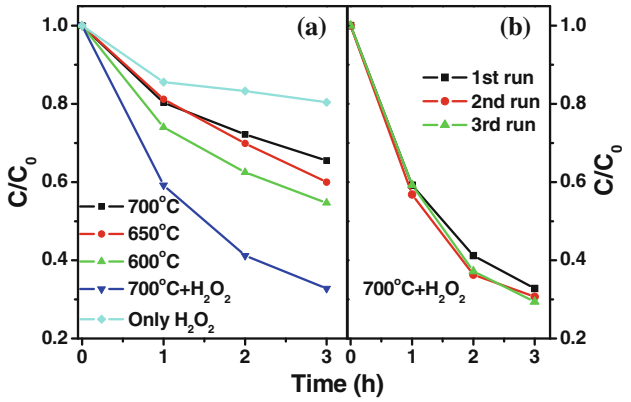

Fig. 5 Photocatalysis of $Bi_2Fe_4O_9$ nanofibers on degradation of MO under visible irradiation

of irradiation time under visible light illumination. The degradation of the MO without any photocatalyst under the visible light irradiation for 3 h was less than 10 %, which was not shown in the figure. Evidently, it could be observed from Fig. 5a that the three samples exhibited different degradation behaviors after the visible light irradiation. The $Bi_2Fe_4O_9$ nanofibers annealed at 700 °C exhibited favorable degradation efficiency of about 35 %. However, better efficiency of 40 and 45 % was obtained for the samples annealed at 650 and 600 °C, respectively. It could be concluded that the $Bi_2Fe_4O_9$ nanofibers annealed at lower temperatures seemed more active. The three samples exhibited the similar bandgap value, but different morphology and optical absorption ability, thus leading to different photocatalytic activities.

It is well known that the photo-induced electron-hole (e-h) pairs are responsible for the photocatalytic reaction and the reaction usually occurs at the interface between the catalyst surface and the reagent. When the e-h pairs are generated in the catalyst, they would transfer through a distance to the catalyst surface to participate in the redox reaction with the reagent. More e-h pairs would be generated in the nanofibers annealed at 700 °C because of obviously higher light absorption in the wavelength smaller than 500 nm, as can be clearly observed in the Fig. 4a. However, the recombination could occur before the e-h pairs reach the surface in most of the photocatalysts. The higher recombination rate usually leads to a lower photocatalytic activity. For the $Bi_2Fe_4O_9$ nanofibers annealed at different temperatures, different morphology and diameters could be clearly observed in the SEM figures. Nanofibers annealed at 700 °C were rougher and had much larger diameters than the samples annealed at 600 and 650 °C, respectively. Therefore, it would take more time and transfer a longer distance for the e-h pairs to reach the fiber surface, which would result in a higher recombination rate. It could be deduced that less e-h pairs would transfer to the surface of the 700 °C annealed nanofiber, even though more e-h pairs were generated in the sample.

To confirm the speculation about the recombination of the generated e-h pairs, photoluminescence spectra were recorded for the three samples annealed at different temperatures. As shown in Fig. 6, the samples exhibited different fluorescence intensity at an excitation of 210 nm. There are several emission peaks for the sample and they are located at the same wavelength. However, the intensity of the samples was not in the regular pattern, so the integrated intensity of the fluorescence was used to compare the photoluminescence property of the three samples. Before the integration, the wavelength of the fluorescence was transformed to the energy of the light. The inset figure of Fig. 6 displays the relative ratio of the integrated intensity for the three samples and the integrated intensity of the 700 °C annealed sample was used as a reference. The nanofibers annealed at 700 °C showed the highest intensity which could be assigned to the more recombination caused

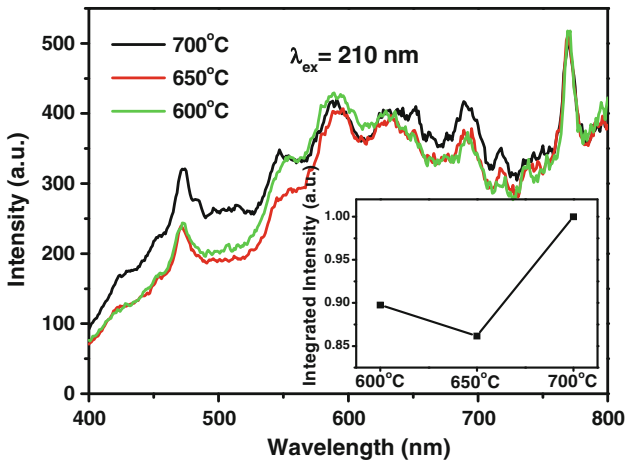

Fig. 6 PL spectra of the $Bi_2Fe_4O_9$ nanofibers annealed at different temperatures. The *Inset* figure shows the relative integrated intensity of the fluorescent light for the three samples

by the much larger diameter and it was consistent with the previous speculation. Even though more recombination existed in the 700 °C annealed sample, favorable photocatalytic efficiency could be obtained because of the higher light absorption as detected in Fig. 4, which was beneficial to the generation of e-h pairs. However, the sample annealed at 650 °C displayed lower intensity when compared with the sample annealed at 600 °C. The main reason could be assigned to the smaller amount of $BiFeO_3$ that existed in the sample, which could also be detected from Fig. 2.

Besides the e-h recombination, the surface area of the catalyst is also an important factor that affects its catalytic activity [43, 44]. The BET specific surface area (m^2/g), the effective surface area (m^2) in the photocatalytic reaction, and the phase state of the $Bi_2Fe_4O_9$ nanofibers annealed at different temperatures are shown in Table 1. The BET specific surface area was 7.268, 6.004, and 3.816 m^2/g for the sample annealed at 600, 650, and 700 °C, respectively. It could be noted that the nanofiber with the smallest diameter offered the larger surface area and the surface area decreased obviously with the increase of the fiber diameter. Then, it could be concluded that the best photocatalytic activity of the 600 °C annealed nanofibers could be mainly attributed to the large specific surface area and relatively low recombination of the e-h pairs.

To improve the photocatalytic activity, reducing the recombination of the e-h pairs is an effective way. It has been demonstrated that there exists a middle narrow band between the conduction band and the valence band [21]. Usually, the middle band in the $Bi_2Fe_4O_9$ may serve as a charge recombination center and limit the catalysis efficiency. To improve the degradation efficiency, H_2O_2, which usually benefits to the photocatalytic activity of ferric oxides [21, 45], was introduced into the reaction

Table 1 Specific surface area, effective surface area in the photocatalytic reaction, and phase state of the electrospun $Bi_2Fe_4O_9$ nanofibers annealed at different temperatures

Annealing temperature	600 °C	650 °C	700 °C
Specific surface area (m^2/g)	7.268	6.004	3.816
Effective surface area (m^2)	0.2907	0.2401	0.1526
Phase state	$Bi_2Fe_4O_9(BiFeO_3)$	$Bi_2Fe_4O_9(BiFeO_3)$	$Bi_2Fe_4O_9$

solution at a concentration of 50 mg/L. After irradiation for 3 h under visible light, a better efficiency up to 70 % could be obtained for the pure-phase sample with the aid of H_2O_2, as can be seen in Fig. 5a. Blind test with only H_2O_2 in the MO solution was also conducted, and the degradation efficiency was about 20 % after irradiation for 3 h. It can be seen that the efficiency up 70 % is much higher than the summation of the efficiency for the pure-phase sample and only H_2O_2 in the MO solution. The enhancement of the photocatalytic activity could be mainly ascribed to the following reaction process:

$$H_2O_2 + Bi_2Fe_4O_9\ (e^-) \rightarrow {}^{\bullet}OH + OH^-$$

From the above equation, it could be concluded that H_2O_2 acts as an electron scavenger, which could lead to a faster degradation of MO and prevent the e-h recombination. The photocatalytic efficiencies of $Bi_2Fe_4O_9$ with different morphologies prepared through different methods are listed in Table 2. The polycrystalline nanofibers annealed at 700 °C show a slightly higher efficiency, compared with single-crystal microplates, nanosheets, and nanoplates without the aid of H_2O_2 [20–23]. The result might be related to the one-dimensional porous structure of the sample, which should be beneficial to the photocatalytic activity. However, the efficiency of the single-crystalline $Bi_2Fe_4O_9$ nanocrystals with specific surfaces could reach 90 % over the organic pollutant of methyl blue irradiation for 4 h with the aid of H_2O_2 [24]. The higher efficiency could be ascribed to the single-crystalline phase with specific surfaces and the aid of H_2O_2, inducing a Fenton reaction beneficial to the photodegradation efficiency [21, 45]. The degradation efficiency in our experiment was enhanced by about 35 %, which was low compared to the report by Sun [21]. The lower enhancement could be ascribed to the lower effect of electron scavenging as H_2O_2 reacts with the polycrystalline $Bi_2Fe_4O_9$ nanofibers.

Moreover, cycling uses as well as maintaining high photocatalytic activity should be a critical issue for long-term use in practical photocatalytic applications. The stability of the photocatalyst to maintain its high activity is a

Table 2 Photocatalytic efficiency and morphology of $Bi_2Fe_4O_9$ prepared through different methods

Degradation pollutant	Bandgap/eV	Efficiency	Time and illumination	Morphology of the photocatalyst
MO	2.0	80 %	25 h/400 W Metal-halide lamp	Nanosheet [20]
Phenol	2.04	30 % 74 %/H_2O_2	4 h/500 W Xe lamp	Nanoplate [21]
MO	No mention	6 %	1 h/250 W Metal-halide lamp	Nanosheet, Nanoplate [23]
MB	1.91 ~ 2.04	90 %/H_2O_2	4 h/500 W Xe lamp	Nanocrystals [24]
MR	2.08	40 %	6 h/20 W tri-phosphor fluorescent lamp	Nanoparticle [22]
MO	2.1	35 % 70 %/H_2O_2	3 h/400 W Metal-halide lamp	Nanofiber [this study]

key factor for an excellent photocatalyst, since the photocorrosion and photodissolution of the catalyst might occur on the photocatalyst surface during the photocatalytic reaction. To test the stability of the $Bi_2Fe_4O_9$ nanofibers, we repeatedly used the catalyst for three times and the results are shown in Fig. 5b. Each experiment was carried out under identical conditions and the photocatalytic activity of the $Bi_2Fe_4O_9$ nanofibers remained almost the same in the three cycling experiments. Besides the stability, the large length/diameter ratio of the one-dimensional $Bi_2Fe_4O_9$ nanofiber would facilitate its separation from the solution.

The above results demonstrate that the pure-phase electrospun $Bi_2Fe_4O_9$ nanofiber could be an excellent photocatalyst with a favorable degradation capacity under the visible light irradiation. Enhanced efficiency could be obtained by adding H_2O_2 to reduce the recombination of the e-h pairs. Moreover, the stability of the $Bi_2Fe_4O_9$ nanofibers after cycling experiments was also confirmed. It is indicated that the electrospun $Bi_2Fe_4O_9$ nanofibers would be a promising candidate for the visible light photocatalyst.

Conclusions

In summary, $Bi_2Fe_4O_9$ nanofibers were successfully synthesized by electrospinning in combination with a typical sol–gel method. The as-spun nanofibers were continuous and uniform with a diameter of 320 nm. After annealing at different temperatures, the morphology changed with different temperatures. The diameter was reduced to 150 and 180 nm after annealing at 600 and 650 °C, respectively. However, the diameter increased to 250 nm and some nanofibers were broken into short fibers after annealing at 700 °C. The annealed $Bi_2Fe_4O_9$ nanofibers showed visible light absorption and the bandgap values were determined to be around 2.1 eV. $Bi_2Fe_4O_9$ nanofibers annealed at 600 °C exhibited a favorable efficiency of 45 % and it was higher than that of the other samples, which could be mainly attributed to the low recombination of e-h pairs and higher surface area. The degradation efficiency over the organic pollutant MO was determined to be 70 % for the pure-phase nanofibers annealed at 700 °C with the aid of H_2O_2 under the irradiation of visible light for 3 h. The enhancement could be attributed to the electron scavenging effect of the H_2O_2. Furthermore, the electrospun $Bi_2Fe_4O_9$ nanofiber could recycle for three times without obvious decrease of the photocatalytic activity. The above results indicate that the electrospun $Bi_2Fe_4O_9$ nanofiber might be a promising visible light photocatalyst.

Acknowledgements This study was financially supported by a project of Natural Science Foundation of Anhui Province (1108085J14) and the National Natural Science Foundation of China (50972035 and 51272060).

References

1. Hoffmann MR, Martin ST, Choi W, Bahnemann DW (1995) Chem Rev 95:69
2. Chen XB, Mao SS (2007) Chem Rev 107:2891
3. Wu TX, Liu GM, Zhao JC, Hidaka H, Serpone N (1998) J Phys Chem B 102:5845
4. Wu TX, Liu GM, Zhao JC, Hidaka H, Serpone N (1999) J Phys Chem B 103:4862
5. Zhao W, Chen CC, Li XZ, Zhao JC, Hidaka H, Serpone N (2002) J Phys Chem B 106:5022
6. Xin YJ, Liu HL, Han L (2011) J Mater Sci 46:7822. doi:10.1007/s10853-011-5763-6
7. Sakthivel S, Kisch H (2003) Angew Chem Int Ed 42:4908
8. Wei HY, Wu YS, Lun N, Zhao F (2004) J Mater Sci 39:1305. doi:10.1023/B:JMSC.0000013889.63705.f3
9. Tang JW, Zou ZG, Ye JH (2004) Angew Chem Int Ed 43:4463
10. Gao F, Chen XY, Yin KB, Dong S, Ren ZF, Yuan F, Yu T, Zou ZG, Liu JM (2007) Adv Mater 19:2889
11. Finlayson AP, Tsaneva VN, Lyons L, Clark M, Glowacki BA (2006) Phys Stat Sol A 203:327
12. Luo JH, Maggard PA (2006) Adv Mater 18:514
13. Poghossian AS, Abovian HV, Avakian PB, Mkrtchian SH, Haroutunian VM (1991) Sensor Actuat B-Chem 4:545
14. Zakharchenko NI (2002) Kinet Catal 43:95
15. Xiong Y, Wu MZ, Peng ZM, Jiang N, Chen QW (2004) Chem Lett 33:502
16. Park TJ, Papaefthymiou GC, Moodenbaugh AR, Mao YB, Wong SS (2005) J Mater Chem 15:2099

17. Singh AK, Kaushik SD, Kumar B, Mishra PK, Venimadhav A, Siruguri V, Patnaik S (2008) Appl Phys Lett 92:132910
18. Ressouche E, Simonet V, Canals B, Gospodinov M, Skumryev V (2009) Phys Rev Lett 103:267204
19. Tian ZM, Qiu Y, Yuan SL, Wu MS, Huo SX, Duan HN (2010) J Appl Phys 108:064110
20. Ruan QJ, Zhang WD (2009) J Phys Chem C 113:4168
21. Sun SM, Wang WZ, Zhang L, Shang M (2009) J Phys Chem C 113:12826
22. Zhang M, Yang H, Xian T, Wei ZQ, Jiang JL, Feng YC, Liu XQ (2011) J Alloy Compd 509:809
23. Zhang XY, Lv J, Bourgeois L, Cui JW, Wu YC, Wang HT, Webley PA (2011) New J Chem 35:937
24. Zhang Q, Gong WJ, Wang JH, Ning XK, Wang ZH, Zhao XG, Ren WJ, Zhang ZD (2011) J Phys Chem C 115:25241
25. Liu ZS, Wu BT, Yin DG, Zhu YB, Wang LG (2012) J Mater Sci 47:6777. doi:10.1007/s10853-012-6600-2
26. Zhao JY, Liu T, Xu YB, He YY, Chen WP (2011) Mater Chem Phys 128:388
27. Liu T, Xu YB, Zeng CL (2011) Mat Sci Eng B 176:535
28. Wang YG, Xu G, Yang LL, Ren ZH, Wei X, Weng WJ, Du PY, Shen G, Han GR (2007) J Am Ceram Soc 90:3673
29. Yang Z, Huang Y, Dong B, Li HL, Shi SQ (2006) J Solid State Chem 179:3324
30. Ramaseshan R, Sundarrajan S, Jose R, Ramakrishna S (2007) J App Phys 102:111101
31. Greiner A, Wendorff JH (2007) Angew Chem Int Ed 46:5670
32. Li D, Xia YN (2004) Adv Mater 16:1151
33. Ramakrishna S, Jose R, Archana PS, Nair AS, Balamurugan R, Venugopal J, Teo WE (2009) J Mater Sci 45:6283. doi:10.1007/s10853-010-4509-1
34. Kim HK, Honda W, Kim BS, Kim IS (2013) J Mater Sci 48:1111. doi:10.1007/s10853-012-6843-y
35. Zhang W, Li HP, Pan W (2012) J Mater Sci 47:8216. doi:10.1007/s10853-012-6717-3
36. Zhang XW, Xu SY, Han GR (2009) Mater Lett 63:1761. doi:10.1007/s10853-006-0241-2
37. Nakane K, Shimada N, Ogihara T, Ogata N, Yamaguchi S (2007) J Mater Sci 42:4031. doi:10.1007/s10853-008-3201-1
38. Chandrasekar R, Zhang LF, Howe JY, Hedin NE, Zhang Y, Fong H (2009) J Mater Sci 44:1198
39. Hu GJ, Meng XF, Feng XY, Ding YF, Zhang SM, Yang MS (2007) J Mater Sci 42:7162. doi:10.1007/s10853-007-1609-7
40. Barakat NAM (2012) J Mater Sci 47:6237. doi:10.1007/s10853-012-6543-7
41. Lin H, Huang CP, Li W, Ni C, Shah SI, Tseng YH (2006) Appl Catal B-Environ 68:1
42. Chiu SC, Li YY (2009) J Cryst Growth 311:1036
43. Qi SS, Zuo RZ, Liu Y, Wang Y (2013) Mater Res Bull 48:1213
44. Bell AT (2003) Science 299:1688
45. Du WP, Xu YM, Wang YS (2008) Langmuir 24:175